

SEISMOLOGY

Illuminating seafloor faults and ocean dynamics with dark fiber distributed acoustic sensing

Nathaniel J. Lindsey^{1,2*}, T. Craig Dawe³, Jonathan B. Ajo-Franklin^{2,4}

Distributed fiber-optic sensing technology coupled to existing subsea cables (dark fiber) allows observation of ocean and solid earth phenomena. We used an optical fiber from the cable supporting the Monterey Accelerated Research System during a 4-day maintenance period with a distributed acoustic sensing (DAS) instrument operating onshore, creating a ~10,000-component, 20-kilometer-long seismic array. Recordings of a minor earthquake wavefield identified multiple submarine fault zones. Ambient noise was dominated by shoaling ocean surface waves but also contained observations of in situ secondary microseism generation, post–low-tide bores, storm-induced sediment transport, infragravity waves, and breaking internal waves. DAS amplitudes in the microseism band tracked sea-state dynamics during a storm cycle in the northern Pacific. These observations highlight this method's potential for marine geophysics.

The underwater environment that covers 70% of Earth's surface poses major logistical challenges to seafloor studies. Marine geophysical research is conducted with large research vessels, temporary ocean-bottom seismometers (1), and a limited number of permanent tethered observatories (2, 3). Emerging float networks, seafloor global navigation satellite system, and high-frequency remote sensing are beginning to infill major data gaps with promising near–real-time cov-

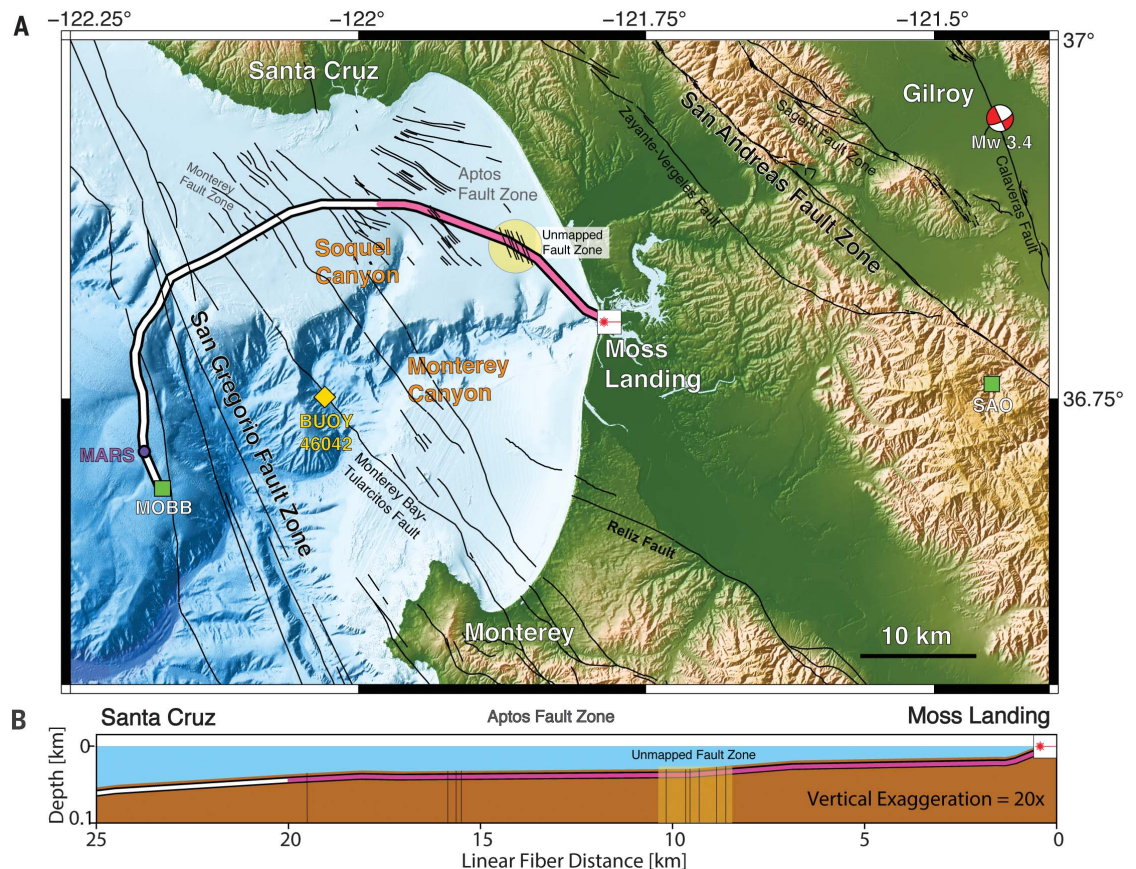
erage. The impact has included quantification of offshore seismic hazards (4, 5), submarine volcanism (6), marine ecology, and ocean transport (7), yet many oceanographic and solid-earth processes remain spatially aliased.

Fiber-optic sensing is an emerging means of recording dense geophysical information onshore (8, 9) and should be equally useful offshore, using existing dark fiber seafloor optical fibers. Marra *et al.* (10) proposed using transmission time-of-flight of ultrastable laser

pulses inside transoceanic subsea fibers to record cable-averaged seafloor strain. To examine seafloor strain with higher spatial resolution, we used backscattered laser pulses with phase-based coherent optical time-domain reflectometry (φ -OTDR), otherwise known as distributed acoustic sensing (DAS), inside the Monterey Accelerated Research System (MARS) science cable that spans the continental shelf offshore of California (Fig. 1) (11). In contrast to the approach of Marra *et al.*, DAS multiplexes the optical analysis and thus resolves the seafloor strain field every 10 m, which in our case produced an array dataset totaling 3.2 TB collected over 4 days.

We recorded the 11 March 2018 strike-slip earthquake near Gilroy, CA, using the MARS cable. Figure 2 shows this earthquake wavefield DAS record after minimal data processing (11). P, pP, PP, S, and SS phase arrivals matched predicted arrival times for the U.S. Geological Survey–cataloged event solution and

Fig. 1. MARS DAS experiment. (A) Map of Monterey Bay, CA, shows MARS cable (DAS, pink portion), mapped faults, Gilroy earthquake (red-and-white beach ball), seismometers BK.SAO and BK.MOBB (green squares), NOAA buoy 46042 (yellow diamond), and major bathymetric features. (B) Cross-section illustration of MARS cable used for DAS.



¹Earth and Planetary Science Department, University of California, Berkeley, 300 McCone Hall, Berkeley, CA 94720, USA. ²Energy Geosciences Division, Lawrence Berkeley National Laboratory, 1 Cyclotron Road, Berkeley, CA 94720, USA. ³Monterey Bay Aquarium Research Institute, 7700 Sandholdt Road, Moss Landing, CA 95039, USA. ⁴Department of Earth, Environmental, and Planetary Sciences, Rice University, MS-126, 6100 Main Street, Houston, TX 77005, USA. *Corresponding author. Email: natelindsey@berkeley.edu

cable geometry. The P-wave was barely visible over cable segments, potentially owing to the suboptimal orientation of particle motion relative to the fiber axis ($\theta > 71^\circ$). Converted pP and PP phases with greater horizontal components were more robustly observed. Time-domain beamforming of the record found that energy arrived with equal components from the epicentral backazimuth of 81°N and a direction around 45°N (Fig. 2E), interpreted as seismic multipathing through the complex three-dimensional North American–Pacific plate boundary (12). A second source of scattering was found to originate from local structure immediately below the seafloor cable.

After each seismic phase, we observed strong coherent seismic energy propagating outward with apparent velocity of 200 to 600 m/s from discrete points between 15.1 and 16.3 km on the MARS cable and also between 8.4 and 10.3 km (Fig. 2, B to D). We interpreted this as body

wave conversion into Scholte waves at subvertical seafloor faults, which act as point scatterers. Scholte waves have Rayleigh-type wave motion and propagate at the ocean–solid earth interface. Wavefront tracking of the main SS phase showed slowdown between 14.5 and 16.5 km, coincident with observed scattering (Fig. 2D). Assuming wave propagation in the cable axis plane, velocity decreased from 2.1 km/s to 1.2 km/s over <1 km. We interpreted this as a waveguide effect where seismic energy interacts with highly fractured, low-velocity fault zone gouge layers (13). Similar observations were made for the subsequent magnitude 2.7 aftershock.

Recent high-resolution seismic reflection imaging from this section of the continental shelf near Monterey and Soquel canyons identified extensive paleocanyon deposits and the NW–SE striking Aptos Fault Zone, a major step-over relay between the San Andreas Fault

Zone onshore and the San Gregorio Fault Zone offshore (14, 15). Four subvertical Aptos faults mapped in (14) transect the MARS cable around 15 to 17 km and near 19 km at an oblique angle (Fig. 1). These fault locations correlate with observed secondary scattering locations from the Gilroy event. We identified a number of unmapped faults (Fig. 1 for locations; strike based on regional information) in a segment extending the Aptos Fault Zone 15 to 20 km SSE parallel to shore, potentially connecting to the Monterey Canyon.

Ocean–solid earth interactions generate Rayleigh waves between 0.05 and 0.5 Hz, which are globally recorded as primary and secondary microseisms (16–19). In principle, horizontal seafloor fibers have zero strain sensitivity to primary microseism (PM) hydrostatic load changes. To test this hypothesis, we fit a PM model based on buoy wave height records to DAS strain data at 0.05 to 0.15 Hz (11). We

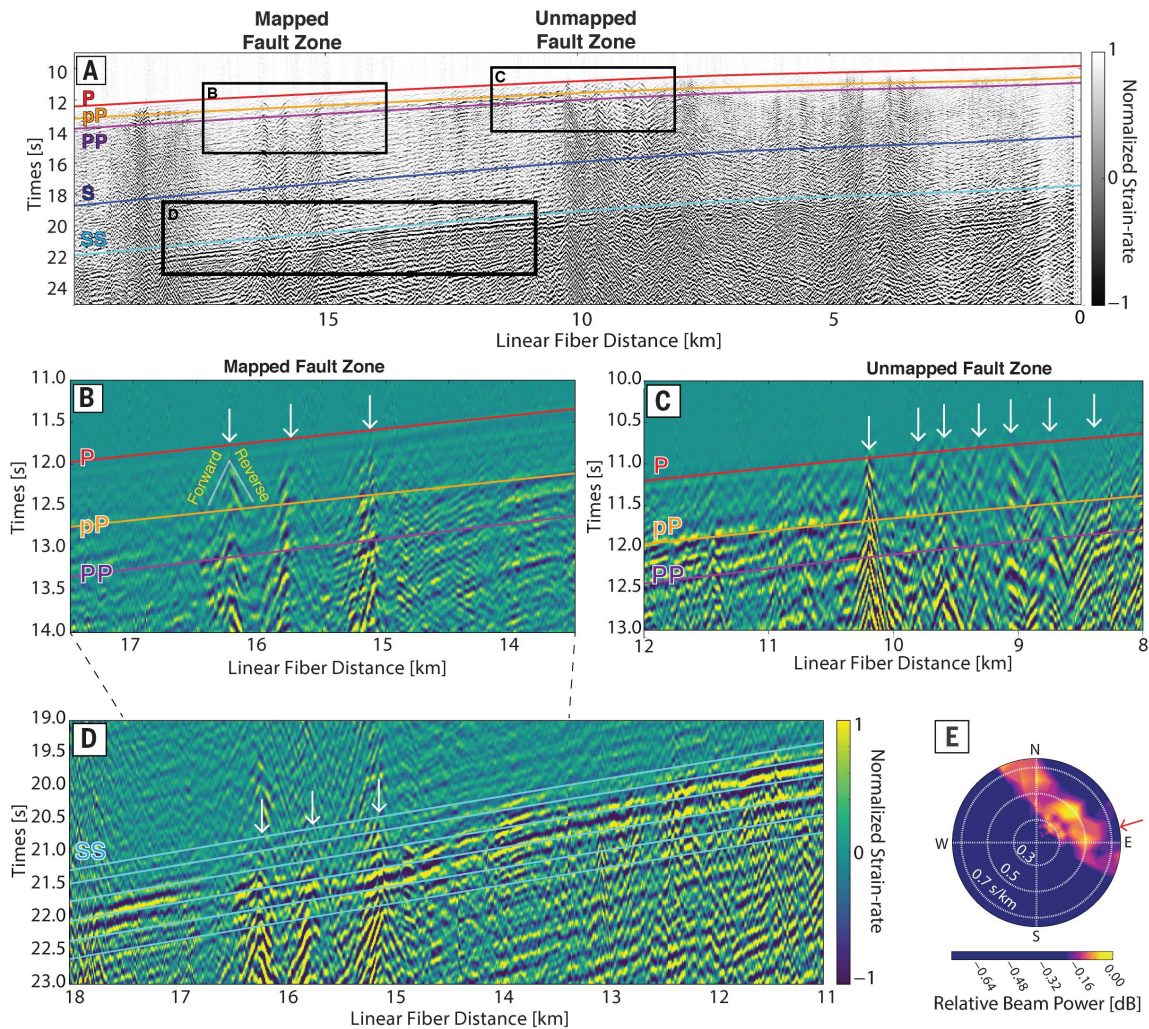


Fig. 2. Magnitude 3.4 11 March 2018 Gilroy earthquake wavefield. (A) Full array observation (0 indicates the shore) with predicted seismic phase arrivals (colored lines). (B) Inset shows scattering with recently mapped submarine fault locations (white arrows). (C) Same as (B), for an unmapped fault zone.

(D) Observed 0.25-s wavefront delay in mapped fault zone from (B). Lines show predicted constant phase arrivals immediately after the first SS wavefront. (E) Time-domain beamforming solution shows energy arriving from ENE azimuths, while red arrow shows predicted backazimuth.

found that these DAS records can be explained as PM (fig. S1), likely because the fiber package experiences a Poissonian strain response (20) or an unquantified transverse seafloor current motion in the shallow waters of Monterey Bay.

Tracking microseism energy over 4 days (Fig. 3), we observed a consistent response between buoy wave motion, seafloor DAS strain,

and seismometer noise onshore (21). All three instruments record high amplitudes during the initial period of high storm activity on 10 March 2018. Recorded amplitudes decrease as the first storm loses energy and then increase as the second storm builds. Small absolute frequency shifts and amplitude discrepancies between the three records could

be the result of a number of variables, including complicated energy partitioning, that is, the quality and character of microseism energy conversion at the ocean-continent interface; fiber and seismometer coupling; lateral separation and water-depth differences between the buoy and fiber (18); and poorly constrained ocean site effects (21).

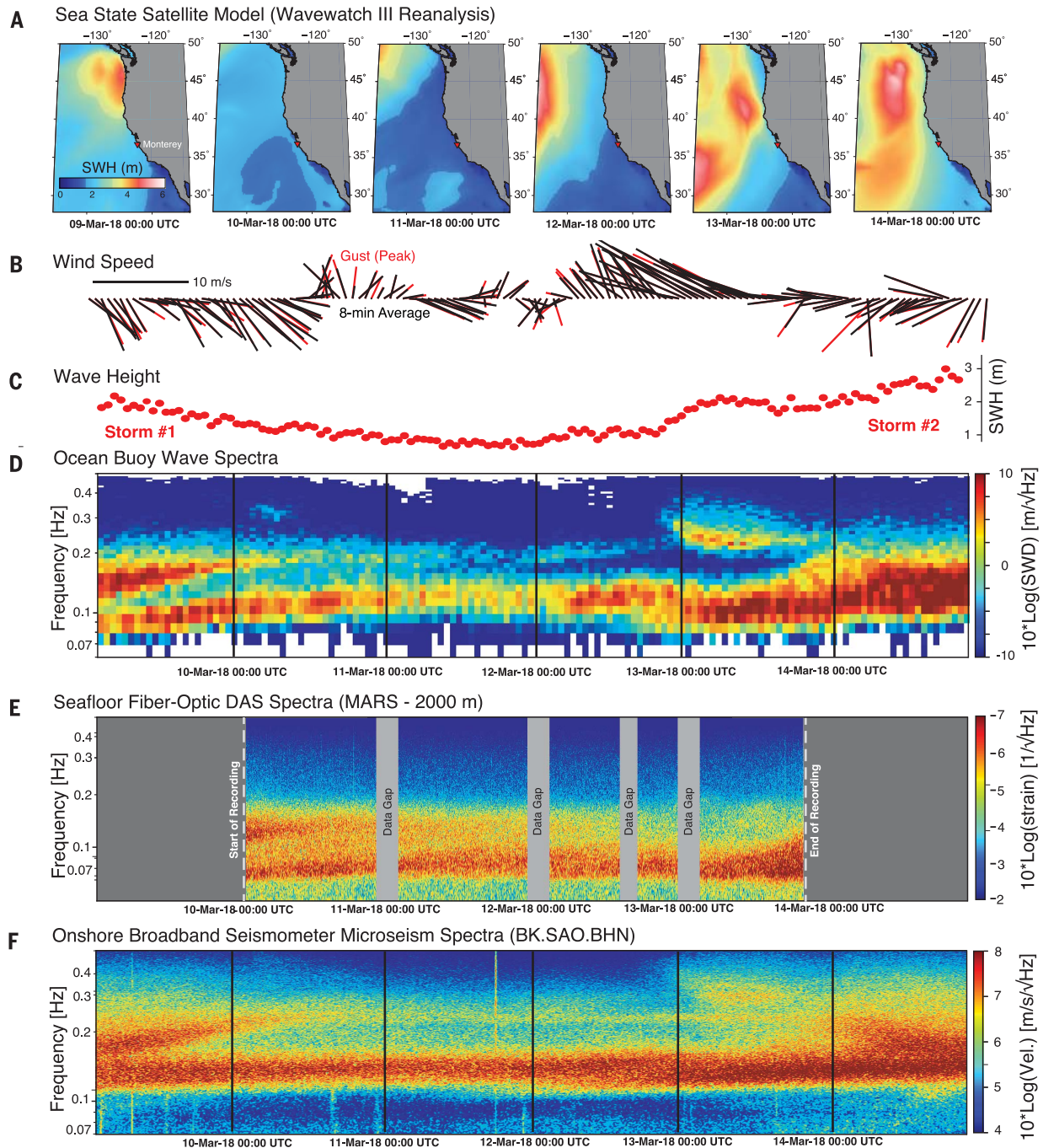


Fig. 3. Multi-instrument analysis of sea-state evolution. (A) Wavewatch III reanalysis of satellite remote-sensing data shows ocean wave height outside Monterey Bay (red triangle). (B to D) NOAA buoy 46042 8-min average measurements of wave speed and direction (black) and peak gust (red), and 10-min average wave height and spectral wave density (SWD) measurements.

(E) Seafloor DAS strain from cable location 2 km averaged over a 15-min sliding window. (F) North component of ground velocity from onshore broadband inertial seismometer BK.SAO averaged over a 15-min sliding window. Buoy, DAS, and seismometer measurements show time-lapse interactions of primary and secondary ocean microseism between two Pacific storm cycles.

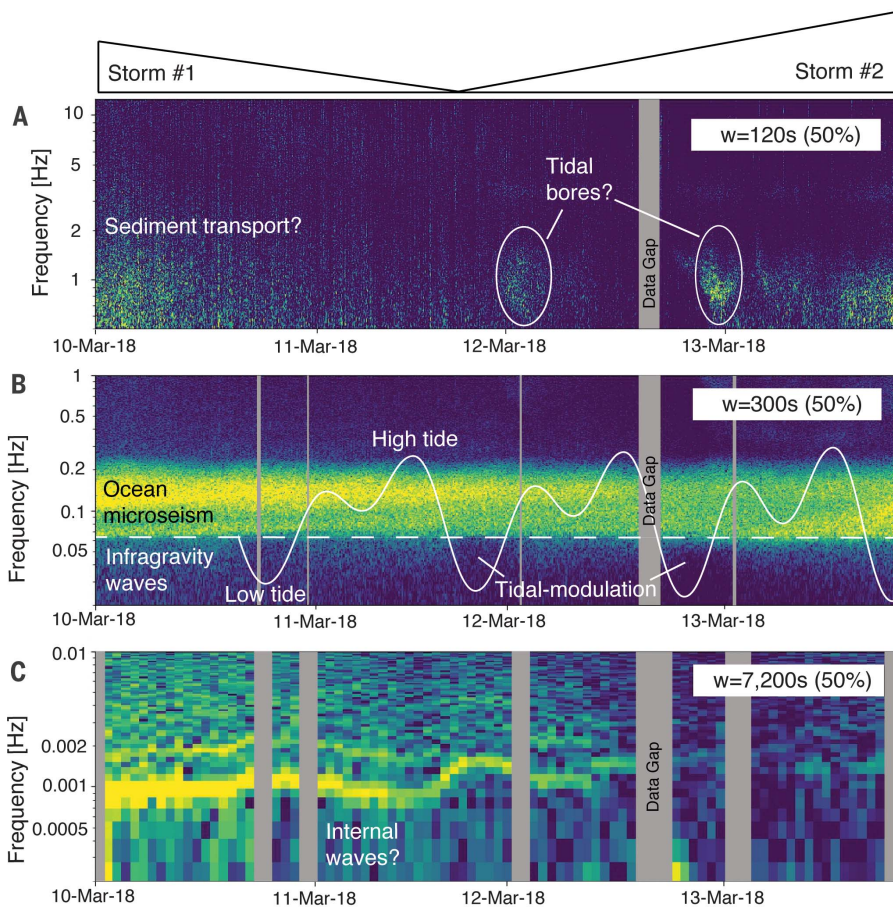


Fig. 4. Broadband hydrodynamic signals. DAS data for cable location 5.5 km analyzed with a sliding window (w) of 120-, 300-, or 7200-s duration, 50% overlap. **(A)** 0.5 to 11 Hz: high-frequency noise consistent with timing of expected storm-induced sediment transport (see Fig. 3A for storm activity) and tidal bore activity. **(B)** 0.02 to 1 Hz: primary and secondary microseism observations changing energy with storm activity, with tidally modulated infragravity noise below 0.05 Hz; NOAA tide gauge 9413745 from Santa Cruz, CA, plotted for reference (mean lower low water level minimum = -0.03 m, maximum = 1.42 m). **(C)** 0.0002 to 0.01 Hz: tidally modulated harmonic noise, potentially caused by bay seiche or breaking internal waves at the continental shelf. Data gaps change with window duration.

To assess energy partitioning, we decomposed the wavefield in the frequency-wavenumber domain. Shoaling wave loads in shallow water produce PMs (18, 22) that obey the dispersion equation

$$\omega^2 = g k \tanh(kH)$$

where ω is angular frequency, g is gravitational acceleration, k is wavenumber, and H is water depth. DAS PM recordings were found to be strongly dispersive (fig. S2). Because PMs are caused by local wave height, outgoing components are the result of coast reflection. We thus computed that the reflected PM energy is $\sim 1\%$ of the incoming energy.

The leading hypothesis for secondary microseism (SM) generation is that opposing wind-wave trains mix nonlinearly and produce Scholte waves at near-acoustic speeds (23, 24).

Testing this hypothesis requires observation of both opposing ocean waves and the resulting Scholte wave generation, which has only been documented in one deep-ocean environment (25). In Monterey Bay, we observed weak energy at 0.25 to 1.5 Hz and very low wavenumber (0.003 m^{-1}) with symmetric amplitude components traveling at 400 to 1000 m/s, faster than observed wind-wave speeds. We interpreted this as in situ SM generation ultimately produced by the nonlinear interaction of the aforementioned incoming and outgoing wind-waves (fig. S2C). This suggests that SMs are generated even when one wind-wave component is vanishingly small. SM amplitudes were 1.5 to 2 dB below PM, likely owing to the shallow water environment.

We detected a number of nonmicroseism hydrodynamic signals (Fig. 4). At 0.5 to 5 Hz, we observed decreasing amplitude as the first

storm lost energy, consistent with seafloor current-driven sediment transport similar to noise profiles of bedload transport observed onshore near rivers (26, 27). At 1 to 2 Hz, we observed transients coincident with rising tide, interpreted as thermal strain related to semi-diurnal internal tidal bores (28–31). At 0.005 to 0.05 Hz, we observed tidally modulated infragravity waves previously observed using the Monterey Bay seismometer supported by MARS (32). At ~ 0.001 Hz, we also observed a strong gliding signal with harmonics declining in energy from 10 March 2018. Signal gliding correlated with high and low tide. The signal may be related to the higher harmonics of the Monterey Bay seiche (33), but water level monitoring documented stable seiche amplitudes (34). An alternative hypothesis is that this is a solid-earth tilt response to slow-moving internal gravity waves, vertical oscillations of the ocean stratification interface, which break near steep bathymetric features such as the Monterey Canyon (28, 35–37). Internal waves enhance cross-shelf transport of fluid and biology and are therefore foundational in models of thermohaline ocean circulation and marine ecology (38). Independent of the source mechanism, this low-frequency DAS signal highlights the potential utility of the method for studying quasi-geodetic strain phenomena.

REFERENCES AND NOTES

1. C. Deplus *et al.*, *Geology* **26**, 131 (1998).
2. B. Romanowicz, P. McGill, D. Neuhauser, D. Dolenc, *Seismol. Res. Lett.* **80**, 197–202 (2009).
3. J. Trowbridge *et al.*, *Front. Mar. Sci.* **6**, 74 (2019).
4. E. Gràcia, J. Dañobeitia, J. Vergés, P. A. R. S. I. F. A. L. Team, *Geology* **31**, 83 (2003).
5. S. Ruiz, R. Madariaga, *Tectonophysics* **733**, 37–56 (2018).
6. T. Mittal, B. Delbridge, *Earth Planet. Sci. Lett.* **511**, 105–116 (2019).
7. L. A. Levin *et al.*, *Front. Mar. Sci.* **6**, 241 (2019).
8. P. Jousset *et al.*, *Nat. Commun.* **9**, 2509 (2018).
9. J. B. Ajo-Franklin *et al.*, *Sci. Rep.* **9**, 1328 (2019).
10. G. Marra *et al.*, *Science* **361**, 486–490 (2018).
11. Materials and methods are available as supplementary materials.
12. A. J. Rodgers, A. Pitarka, N. A. Petersson, B. Sjögreen, D. B. McCallen, *Geophys. Res. Lett.* **45**, 739–747 (2018).
13. Y.-G. Li, P. Leary, K. Aki, P. Malin, *Science* **249**, 763–766 (1990).
14. S. Y. Johnson *et al.*, *Ocean Coast. Manage.* **140**, 88–104 (2017).
15. K. L. Maier, S. Y. Johnson, P. Hart, *Mar. Geol.* **404**, 24–40 (2018).
16. R. A. Haubrich, K. McCamy, *Rev. Geophys.* **7**, 539 (1969).
17. T. Herbers, R. Guza, *J. Phys. Oceanogr.* **21**, 1740–1761 (1991).
18. P. D. Bromirski, F. K. Duennebier, *J. Geophys. Res. Solid Earth* **107**, 2166 (2002).
19. J. Zhang, P. Gerstoft, P. D. Bromirski, *Geophys. Res. Lett.* **37**, L15301 (2010).
20. M. Becker, C. Ciervo, M. Cole, T. Coleman, M. Mondanos, *Geophys. Res. Lett.* **44**, 7295–7302 (2017).
21. L. Gualtieri *et al.*, *Geophys. J. Int.* **197**, 1096–1106 (2014).
22. S. C. Webb, *Rev. Geophys.* **36**, 105–142 (1998).
23. M. S. Longuet-Higgins, *Philos. Trans. R. Soc. London Ser. A* **243**, 1–35 (1950).
24. K. Hasselmann, *Rev. Geophys.* **1**, 177 (1963).
25. E. Muzert, *Geophysics* **72**, U21–U26 (2007).
26. L. Hsu, N. J. Finnegan, E. E. Brodsky, *Geophys. Res. Lett.* **38**, L13407 (2011).

27. B. Schmandt *et al.*, *Geology* **45**, 299–302 (2017).
28. G. S. Carter, M. C. Gregg, R.-C. Lien, *Cont. Shelf Res.* **25**, 1499–1520 (2005).
29. R. K. Walter, C. B. Woodson, R. S. Arthur, O. B. Fringer, S. G. Monismith, *J. Geophys. Res. Oceans* **117**, C07017 (2012).
30. F. Cazenave, Y. Zhang, E. McPhee-Shaw, J. G. Bellingham, T. P. Stanton, *Limnol. Oceanogr. Methods* **9**, 571–581 (2011).
31. J. A. Colosi, N. Kumar, S. H. Suanda, T. M. Freismuth, J. H. MacMahān, *J. Phys. Oceanogr.* **48**, 123–143 (2018).
32. D. Dolenc, B. Romanowicz, D. Stakes, P. McGill, D. Neuhauser, *Geochem. Geophys. Geosyst.* **6**, Q09002 (2005).
33. L. C. Breaker, Y. Tseng, X. Wang, *Prog. Oceanogr.* **86**, 380–395 (2010).
34. J. Park, W. Sweet, R. Heitsenrether, *Ocean Sci.* **11**, 439–453 (2015).
35. C. Garrett, W. Munk, *Annu. Rev. Fluid Mech.* **11**, 339–369 (1979).
36. W. S. Holbrook, I. Fer, *Geophys. Res. Lett.* **32**, L15604 (2005).
37. E. Kunze, L. K. Rosenfeld, G. S. Carter, M. C. Gregg, *J. Phys. Oceanogr.* **32**, 1890–1913 (2002).
38. M. H. Alford *et al.*, *Nature* **521**, 65–69 (2015).
39. N. J. Lindsey, njlindsey/Photonic-seismology-in-Monterey-Bay-Dark-fiber1DAS-illuminates-offshore-faults-and-coastal-ocean: doi generation, Version 1, Zenodo (2019); doi.org/10.5281/zenodo.3475631.

ACKNOWLEDGMENTS

We thank D. Dreger, B. Romanowicz, S. Holbrook, L. Retailleau, L. Gualtieri, T. Mittal, S. Maurya, D. Neuhauser, C. Paull, three anonymous reviewers, and the editor for their insight. We thank Silixa for long-term support of our DAS acquisitions. **Funding:** N.J.L. was supported by NSF GRFP (DGE 1106400). J.B.A.-F. was supported by LBNL Laboratory Directed Research and Development Program (USDOE DE-AC02-05CH11231), which also supported the experiment. Analysis was supported in part by the GoMCarb Project (USDOE DE-AC02-05CH11231). MARS is funded under NSF Award 1514756 with additional support from the David and Lucille Packard Foundation/MBARI.

Author contributions: N.J.L. conceived of and designed the experiment, recorded and analyzed data, and wrote the manuscript. T.C.D. enabled MARS cable access and assisted in field operations. J.B.A.-F. supported the project, contributed to the manuscript, and supervised the project and analysis.

Competing interests: The authors have no competing interests.

Data and materials availability: Data used to generate the figures and support the findings of this manuscript are available at <https://github.com/njlindsey/Photonic-seismology-in-Monterey-Bay-Dark-fiber1DAS-illuminates-offshore-faults-and-coastal-ocean> and in (39).

SUPPLEMENTARY MATERIALS

science.sciencemag.org/content/366/6469/1103/suppl/DC1

Materials and Methods

Figs. S1 and S2

References (40–51)

1 July 2019; accepted 8 October 2019

10.1126/science.aay5881

illuminating seafloor faults and ocean dynamics with dark fiber distributed acoustic sensing

Nathaniel J. Lindsey, T. Craig Dawe and Jonathan B. Ajo-Franklin

Science **366** (6469), 1103-1107.
DOI: 10.1126/science.aay5881

Marine observations with optics

Placing sensors on the seafloor is difficult, but a sensor network has huge potential for observing processes occurring both below and above the seafloor. Lindsey *et al.* measured acoustic vibrations collected by attaching a laser to the Monterey Accelerated Research System's subsea optical fiber during a maintenance period (see the Perspective by Jousset). Acoustic waves were monitored by changes in laser light along the cable. The observations from just a few days allowed mapping of an unknown fault system and detection of several dynamic processes in the water column above.

Science, this issue p. 1103; see also p. 1076

ARTICLE TOOLS

<http://science.sciencemag.org/content/366/6469/1103>

SUPPLEMENTARY MATERIALS

<http://science.sciencemag.org/content/suppl/2019/11/25/366.6469.1103.DC1>

RELATED CONTENT

<http://science.sciencemag.org/content/sci/366/6469/1076.full>

REFERENCES

This article cites 49 articles, 8 of which you can access for free
<http://science.sciencemag.org/content/366/6469/1103#BIBL>

PERMISSIONS

<http://www.sciencemag.org/help/reprints-and-permissions>

Use of this article is subject to the [Terms of Service](#)

Science (print ISSN 0036-8075; online ISSN 1095-9203) is published by the American Association for the Advancement of Science, 1200 New York Avenue NW, Washington, DC 20005. The title *Science* is a registered trademark of AAAS.

Copyright © 2019 The Authors, some rights reserved; exclusive licensee American Association for the Advancement of Science. No claim to original U.S. Government Works